



# Microcavity well-plate for automated parallel bioelectronic analysis of 3D cell cultures

Franziska D. Zitzmann<sup>a,b</sup>, Sabine Schmidt<sup>a</sup>, Ronny Frank<sup>a</sup>, Winnie Weigel<sup>a</sup>, Matthias Meier<sup>a,c</sup>, Heinz-Georg Jahnke<sup>a,\*</sup>

<sup>a</sup> Centre for Biotechnology and Biomedicine, Biochemical Cell Technology, Leipzig University, Deutscher Platz 5, D-04103, Leipzig, Germany

<sup>b</sup> b-ACT Matter, Research and Transfer Centre for bioactive Matter, Leipzig University, Deutscher Platz 5, D-04103, Leipzig, Germany

<sup>c</sup> Helmholtz Pioneer Campus, Helmholtz Zentrum Munich, Neuherberg, Germany

## ARTICLE INFO

### Keywords:

Microcavity array technology  
Selective laser etching  
3D cell culture  
Contractile human cardiomyocyte clusters  
Electrochemical impedance spectroscopy  
Field potential monitoring

## ABSTRACT

Three-dimensional (3D) *in vitro* cell culture models serve as valuable tools for accurately replicating cellular microenvironments found *in vivo*. While cell culture technologies are rapidly advancing, the availability of non-invasive, real-time, and label-free analysis methods for 3D cultures remains limited. To meet the demand for higher-throughput drug screening, there is a demanding need for analytical methods that can operate in parallel. Microelectrode systems in combination with microcavity arrays (MCAs), offer the capability of spatially resolved electrochemical impedance analysis and field potential monitoring of 3D cultures. However, the fabrication and handling of small-scale MCAs have been labour-intensive, limiting their broader application. To overcome this challenge, we have established a process for creating MCAs in a standard 96-well plate format using high-precision selective laser etching. In addition, to automate and ensure the accurate placement of 3D cultures on the MCA, we have designed and characterized a plug-in tool using SLA-3D-printing. To characterize our new 96-well plate MCA-based platform, we conducted parallel analyses of human melanoma 3D cultures and monitored the effect of cisplatin in real-time by impedance spectroscopy. In the following we demonstrate the capabilities of the MCA approach by analysing contraction rates of human pluripotent stem cell-derived cardiomyocyte aggregates in response to cardioactive compounds. In summary, our MCA system significantly expands the possibilities for label-free analysis of 3D cell and tissue cultures, offering an order of magnitude higher parallelization capacity than previous devices. This advancement greatly enhances its applicability in real-world settings, such as drug development or clinical diagnostics.

## 1. Introduction

*In vitro* cell culture models have made significant contributions by reducing the need for laboratory animals and advancing biomedical science, pharmacology, clinical trials, and personalized disease care (Wang et al., 2020). However, traditional two-dimensional (2D) cell culture systems, where cells adhere and grow on flat surfaces, fall short of fully replicating the physiological conditions found in *in vivo* tissues. This inadequacy is attributed to the lack of a natural microenvironment that includes cellular communication, cell-cell interactions, or cell-matrix interactions (Costa et al., 2016; LaBarbera et al., 2012).

To address these limitations, three-dimensional (3D) cell culture technologies have been developed, ranging from simple spheroids formed by aggregating one cell type to complex organoids with highly

structured architecture and variable cell types. 3D cell cultures are particularly used in research areas such as tissue engineering, cancer research, or developmental biology. Spheroid cultures already more closely resemble the *in vivo* extracellular microenvironment, which plays a crucial role in cell growth, proliferation, differentiation, migration, and programmed cell death (Habanjar et al., 2021).

In this context, the development of fast, non-invasive, real-time, and label-free analysis technologies are required to enable cost-effective screening approaches for 3D cultures. These methods are particularly requested for drug development in the preclinical phase, for example, in personalized cancer therapy (Pinto et al., 2020). Electrochemical impedance spectroscopy (EIS) is a potent technique that has already been employed for real-time monitoring in high-throughput screening of 2D cell cultures (Eichler et al., 2015; Jahnke et al., 2017; Scott and

\* Corresponding author.

E-mail address: [heinz-georg.jahnke@bbz.uni-leipzig.de](mailto:heinz-georg.jahnke@bbz.uni-leipzig.de) (H.-G. Jahnke).

<https://doi.org/10.1016/j.bios.2024.116042>

Received 31 October 2023; Received in revised form 10 January 2024; Accepted 12 January 2024

Available online 14 January 2024

0956-5663/© 2024 The Authors. Published by Elsevier B.V. This is an open access article under the CC BY-NC-ND license (<http://creativecommons.org/licenses/by-nc-nd/4.0/>).

Peters, 2010). In combination with microcavity arrays (MCAs), it has also been used in numerous studies for 3D cell cultures to analyse different cell systems for drug-dependent cellular changes (Erdmann et al., 2019; Lopez et al., 2018; Zitzmann et al., 2017), and for investigating cell heterogeneity (Zitzmann et al., 2022). Furthermore, MCA technology allows the use of different label-free and non-invasive analysis techniques, such as field potential monitoring and EIS, at least with different measurement systems, in which the MCA has to be transferred (Fleischer et al., 2019). Multi-well plates are well-suited for standardizing and parallelizing large-scale cell analyses in pharmacological test series (Chan et al., 2018; Mulder et al., 2018). The same multi-well format has been described for impedance-based microelectrode arrays with various electrode designs for monitoring 2D cell culture systems responses to drugs (Eichler et al., 2015; Guo et al., 2011; Schmidt et al., 2022). In contrast, MCA systems for the bioelectronic analysis of 3D cultures have been reported with up to 15 microcavities and laborious manual processing (Kloss et al., 2008; Poenick et al., 2014; Zitzmann et al., 2022). Nonetheless, to empower 3D cell culture systems for MCAs analysis, a compatible biosensor system is required.

In this study, we developed an MCA-based biosensor system in a 96-microwell plate format for the parallel analysis of 3D cell cultures. The MCA platform was fabricated with an SLE process in fused silica, where cavity sizes for holding the 3D cell cultures varied. Upon using transparent fused silica high-resolution optical imaging of the 3D cell cultures was possible next to biosensor analytic operations. Integration of microelectrodes within microcavities for label-free impedance spectroscopy was achieved with a lift-off sputter process. To eliminate the need for manual alignment of 3D cell cultures in the microcavities, an additional plug-in positioning tool was devised and validated. The capabilities of our 96-well plate MCA-based platform were demonstrated measuring real-time impedance responses of human melanoma and human pluripotent stem cell derived-cardiomyocytes in response to drug stimulation.

## 2. Material and methods

### 2.1. Microstructuring of glass wafers using the SLE process

Selective laser-induced etching (SLE) process was used to microstructure 96 cavities in fused silica glass. The cavity layouts were designed using standard CAD software (Autodesk Inventor Professional, 2018; USA). Microcavity designs were implemented as an inverted frustum of a pyramid with a height of 2/3 of the side length 500  $\mu\text{m}$  and a square base. The designs were converted to machine code using Alphacam 2017 R2 CAM software (Vero Software GmbH, Germany). Afterwards, a glass substrate (6 inch wafer, fused silica, MicroChemicals GmbH, Germany) was placed on a xy-linear translation unit inside the SLE device (FEMTOprint f200aHead 2 PP, Switzerland) and processed with a 1030 nm Yb: YAG laser (pulse energy: 230 nJ; pulse length: 400 fs) in several single steps. Finally, the processed glass substrates were etched in KOH solution (45 wt %, 84 °C) in a pulsed ultrasonic bath.

### 2.2. Structuring and fabrication of the 96-well plate microcavity array

Designed for the 96-microwell plate format, the glass base structured with cavities has a size of 113.5 mm  $\times$  75 mm. In the centre of each well a single cavity (side length 500  $\mu\text{m}$ ) is located respectively. On each of the four cavity sides an electrode with an area of 0.11 mm<sup>2</sup>. One reference electrode (0.2 mm<sup>2</sup>) per well is placed next to a microcavity (SI-Fig. 1). For contacting all electrodes, the conductive paths with a width of 0.05 mm need to be routed to the edge of the glass plate and enlarged there to form a pad (dimensions 0.5 mm–0.7 mm). Electrodes were fabricated using a lift-off process, which is described in the SI part as well as the bonding of the PCB and the 96-microtiter plate to the microelectrode array.

### 2.3. Manufacturing of tailored positioning tools for spheroids

The plug-in tool to place spheroids into the 96 microcavities was designed in Cinema 4D R13 (Maxon Computer GmbH, Germany). To compensate for manufacturing tolerances of the 96-microwell plates, the 8  $\times$  12 funnel array was tailored by 3D-printing to each plate. Due to the fact, that many 3D-printed materials are prone to water absorption during culturing leading to swelling and shape distortion, the plug-in positioning tool was geometrically optimized and printed as a flexible unit. Thereby large dimensions are prevented and the impact of water absorption on geometry accuracy is minimized. Details of the printing process are described in the SI.

### 2.4. Manufacturing of hanging drop plug-in

For high-throughput spheroid generation and processing a 96-well hanging drop plug-in tool was adapted (Hsiao et al., 2012). The tool was divided into two 48-well units, where spacers at the bottom were added to allow the inserts to be rested during cell seeding. The hanging drop plug-in tool was 3D-printed on a Formlabs 3B (Formlabs, USA) in Formlabs Clear V4 resin with 50  $\mu\text{m}$  layer thickness and processed according to Formlabs resin protocol with 20 min UV curing at 60 °C. Upon stacking and gentle tapping each insert of the plug-in tool transferred one hanging droplet with a volume of  $\sim$ 35  $\mu\text{L}$  to a microwell.

### 2.5. Bioelectronic analysis of 3D models

Bioelectronic analyses were performed using a self-developed frontend that provided switchable measurement paths for electrical impedance spectroscopy (EIS), and field potential monitoring (FPM). Further a customized MSX-8 DAQ-system (Sciospec Scientific Instruments, Germany) with 4  $\times$  96 channel amplifier and digitizer cards for FPM and 4 high-precision impedance analyser cards for EIS was integrated in the measuring station. The measurement setup was controlled by software tools written in LabView (National Instruments, USA). Impedance spectroscopy analyses were performed with IMA-Advanced software to record impedance spectra (500 Hz–5 MHz, 51 measurement points,  $\pm$ 10 mV amplitude, 0 V bias potential). For cavity characterization glass beads were used ( $\varnothing$  0.5 mm, Lactan, Germany). Measurement of contraction strength was performed at 100 kHz with 600 samples per second. Field potentials were recorded with the FiPRAT software at a sampling rate of 4 kHz.

### 2.6. Cell culture and generation of 3D models

All cell cultures were maintained at 37 °C, 95% humidity, and 5% CO<sub>2</sub>. The cell line HT-144 (ATCC, USA) was cultivated in RPMI1640 supplemented with 10 % fetal bovine serum, antibiotics (2 U/mL penicillin, 2 mM non-essential amino acid solution, 0.2  $\mu\text{g}/\text{mL}$  streptomycin, 20  $\mu\text{g}/\text{mL}$  gentamycin), and 2 mM GlutaMAX (all from Life Technologies, Germany). 3D spheroids were formed using the hanging drop method with either a Petri dish or the self-developed plug-in tool for a 96-well plate. 2000–5000 cells were used for each drop. To prevent the droplets from drying out during the formation period in the incubator, cover lids or well plates of the respective used approach were filled with PBS. The incubation period lasted 3–7 days depending on the cell number. Subsequently, the generated spheroids were transferred to the 96MCA-MES with the developed positioning tool.

Differentiation of stem cell-derived human cardiomyocyte clusters (hCMCs) was performed as previously described (Fleischer et al., 2019). To test the 96MCA-MES hCMCs with a diameter of 500  $\mu\text{m}$  were used. Details of the immunofluorescence analyses and the compound tests in the 96MCA-MES are described in the SI part.

## 2.7. Data analysis

Impedance signal spectra and maximum amplitudes of glass beads (relative impedance) were calculated from impedance magnitude spectra by a self-developed software (IDAT v3.7) according to  $|Z|_{rel} (\%) = (|Z|_{beads} - |Z|_{blank}) / |Z|_{blank} \times 100$  and determines its maximum. The FiPRAT software was used to automatically detect action potentials in the field potential streams by a dynamic threshold-based algorithm. GraphPad Prism 9 (GraphPad Software, USA) was used for statistical analysis. Significance analyses were performed using ANOVA and Bonferroni post hoc test. Differences between two means with  $p < 0.05$  were considered significant (\*),  $p < 0.01$  very significant (\*\*), and  $p < 0.001$  highly significant (\*\*\*)

## 3. Results and discussion

### 3.1. Development of the 96-well microcavity array system and plug-in positioning tool for 3D cell cultures

The in here developed 96-well MicroCavity Array and MicroElectrode System (96MCA-MES) is shown in Fig. 1. The platform combines two of our previous developments, i.e. a glass-structured microcavities for cell culturing (Kloss et al., 2008; Zitzmann et al., 2022), and a 96-well multielectrode array for the automated bioelectronic analysis of 2D cultures (Eichler et al., 2015; Schmidt et al., 2022). The fabrication of the 96MCA-MES involved three main steps (Fig. 1A), i.e. (i) Microcavity structuring in fused silica substrates ( $75 \times 113.5$  mm) using a selective laser etching (SLE) process, (ii) Electrode (Au) patterning and passivation of SU-8 features using cleanroom-supported lift-off technology, and (iii) Integration of the 96MCA-MES substrate into the multi-well system with a PCB frame for rerouting all electrode contacts and subsequently bonding to a 96-well culturing chamber. On the platform, each well featured one microcavity with an edge length of  $500 \mu\text{m}$  and a depth of  $235 \mu\text{m}$ , suitable for holding spheroids with diameters between  $450$  and  $520 \mu\text{m}$ . Additional details of the cavity design are given in SI-Fig. 1A. On the four walls of each microcavity a semi-circular measuring electrode with areas of  $0.11 \text{ mm}^2$  was deposited. Additionally, one separate circular reference electrode for integrated field

potential monitoring was placed next to each microcavity (Fig. 1B). The holding well-plate array had an 8 by 12 matrix design, where the pitch distance between microcavities was  $9 \text{ mm}$ .

Achieving high-precision alignments between the SLE-produced microcavities and electrode sputter process with deviations of less than  $1 \mu\text{m}$  was a critical challenge. Unlike previously manufactured (Butkutė et al., 2021; Gottmann et al., 2017) SLE structured substrates within our lab (Zitzmann et al., 2022), the 96MCA-MES exhibited a significantly larger area of  $113 \times 75 \text{ mm}$ . Despite our best efforts to optimize the SLE structuring process for the microcavities, we were unable to achieve z and xy-position accuracy with less than  $\pm 10 \mu\text{m}$  deviation over the patterned surface. The resulting offset led to the misalignment of the microelectrode within the subsequential deposition step (SI-Fig. 2A). To overcome this problem and achieve uniform microcavity arrays, we divided the SLE manufacturing process in at least three equally sized sub-areas. Within each area, the SLE structuring operation was preceded by an individual determination of the z-surface focus for the laser. Here, five calibration points were set separately for each operation to enable automatic correction of the z-position, thereby preventing position drifts. While this process increased the manufacturing time, it resulted in the required accuracy (SI-Fig. 2B). In contrast to the z-position offset, xy-position offsets were reproducible and could be corrected by adapting the CAD design. Accounting for both SLE offsets, we successfully fabricated the 96MCA-MES with one microcavity and patterned microelectrodes in each well (Fig. 1C, magnification). To facilitate the connection of the 96MCA-MES, a self-developed frontend was employed, where electrical signals were collected by contact spring-pins from the bottom of the 96MCA-MES.

While seeding 2D cultures is usually done simply by pipetting cell suspensions into each well, positioning 3D cultures within MCA cavities generally requires a laborious manual pipetting step under a stereomicroscope (Zitzmann et al., 2022). To automate this step for the 96-well plate approach, we designed a plug-in positioning tool (Fig. 2). The solution we present is a 96 cone-shaped funnel array with a  $1 \text{ mm}$  opening, where pitch distances between the funnels matched the design of the microcavity array. The plug-in was fabricated using SLA-3D-printing technology. Connecting holding structure of the separate funnels was flexible to enable a simple plug-in process (Fig. 2A,

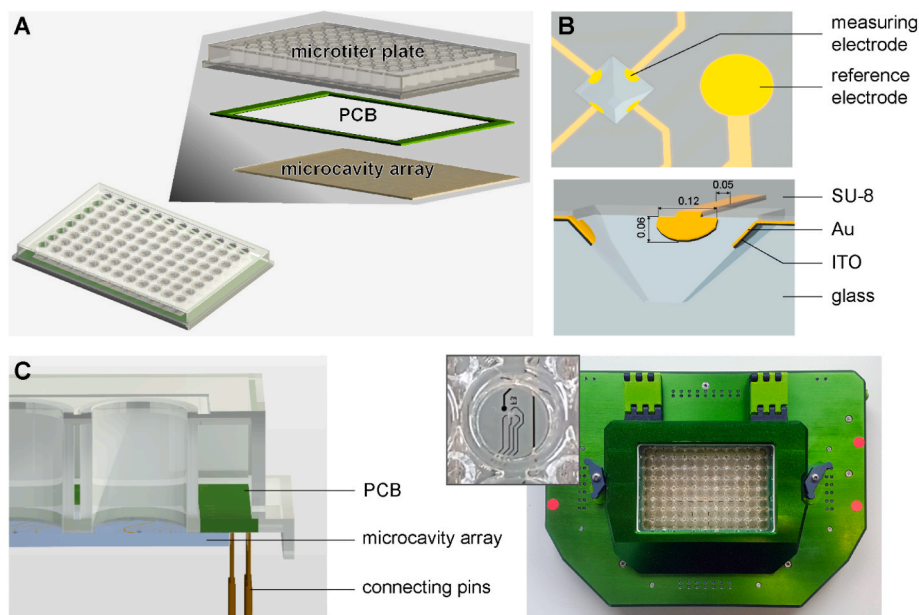


**Fig. 1. Design of the 96-well microcavity array and microelectrode system.** Schematic drawings of the (A) overall and exploded view of the system and (B) one representative microcavity (width/length:  $500 \mu\text{m}$ ) with four semi-circular microelectrodes (dimensions in mm). Next to each microcavity, one circular reference electrode was deposited in each well. (C) Cross-sectional view (left) on the 96MCA-MES with PCB adapter (green) for electrical contacting from the bottom direction. Image (right) shows the self-developed frontend for contacting all single well units of the 96MCA-MES.

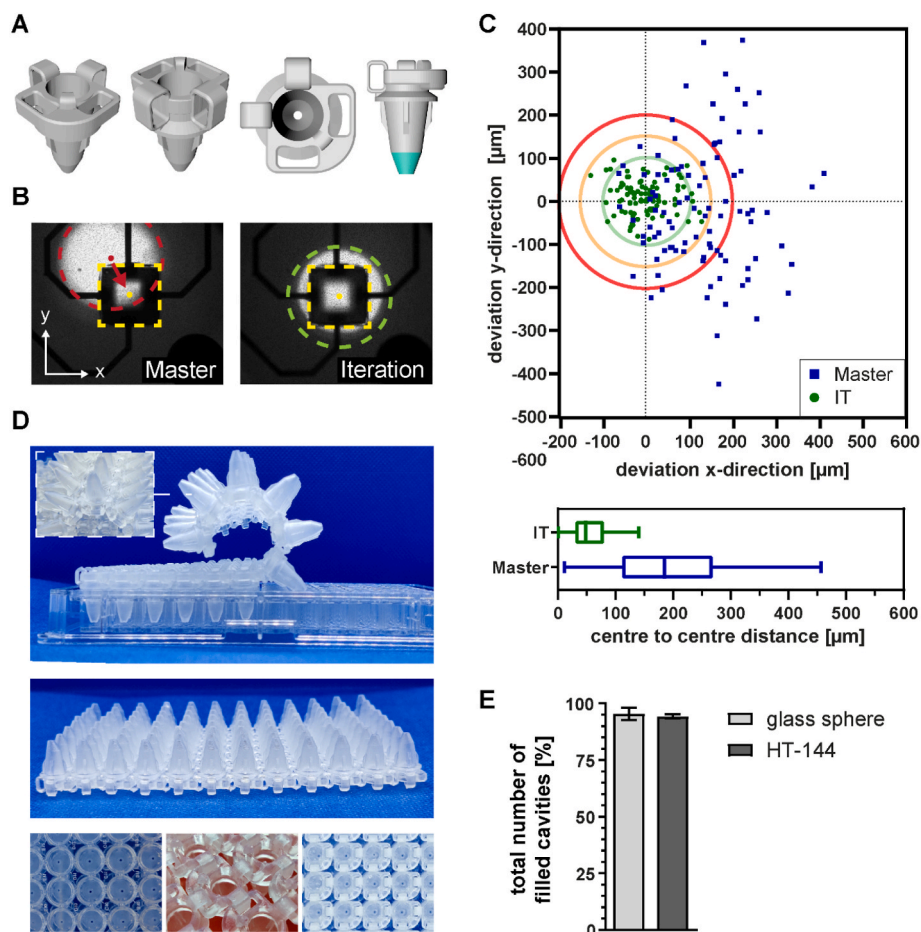


**Fig. 2.** Development of an insert for the automatic positioning of 3D objects in the microcavities of the 96MCA-MES. (A) Design of the funnels from different perspectives. Green denotes the area of the funnel that is individually adjusted in its position according to match the position of the microcavity within the 96MCA-MES. (B) Two-step alignment approach for the funnel guiding structures within the plug-in tool to compensate for position deviations between the microcavity and funnels. (C) Statistical analysis of the alignment deviation between each microcavity and funnels of the master and iterated plug-in tool including individual xy-correction (IT, second step) ( $n = 96$ , boxplot with median, quartile, and min/max). (D) Flexible connecting structure of the plug-in tool. (E) Position test with glass spheres and HT-144 cells showed that over 94 % of the 96MCA were filled correctly (mean  $\pm$  sem,  $n = 3$ ).

SI-Fig. 3). When 3D cultures are pipetted into the funnels, the cell cultures fall into the microcavity by gravity.

Also at this stage, we encountered offsets between the funnel opening and the microcavities exceeding 100  $\mu\text{m}$  without a discernible pattern between individual elements. The reason for this was a variable alignment and straining between the glass substrate with the microcavities and the culture chamber well-plate during the bonding process. To address these manufacturing variations of individual 96MCA-MES, we developed a two-step adaptation strategy. In the first step, the plug-in positioning tool was printed with the given theoretical design parameters (named Master). The plug-in Master was used to determine the deviation from the centre of the cavity to the centre of the funnel opening in the xy-direction (Fig. 2B and C). In the second step, this deviation matrix was used to print a plug-in with corrected funnel coordinates (Fig. 2B, green marked area). By adopting the funnel coordinates to the individual 96MCA-MES, we achieved high alignment accuracy (Fig. 2C). The plug-in positioning tool was printed monolithically (Fig. 2D). The functionality of the corrected plug-in was tested with glass beads and subsequently with HT-144 cell spheroids (Fig. 2E). With the plug-in for 3D object positioning, we achieved filling degrees for the microcavities of  $95.33 \pm 2.67\%$  and  $94.2 \pm 0.97\%$  in three independent experiments with different plates for the glass beads and HT-144 spheroids, respectively. To the best of our knowledge, the 96MCA-MES in combination with the plug-in positioning tool is the first

described solution that allows robust multi-bioelectronic analysis of spheroid cultures.

### 3.2. The 96MCA-MES enables impedimetric analyses of 96 individual 3D objects

For the bioelectronic analyses, we employed a self-developed measurement frontend that enabled the acquisition of electrical impedance spectroscopy (EIS) in a 96-microwell plate format by maintaining the cell culture conditions at 37  $^{\circ}\text{C}$ , 95 % humidity, and 5 %  $\text{CO}_2$ . Initially, we used EIS to confirm the correct functionality of all  $4 \times 96$  micro-electrodes. Impedance spectra were measured in a frequency range from 500 Hz to 5 MHz, with each electrode measured against every other electrode within the individual microcavities. This resulted in six spectra for each microcavity, culminating in a total of 576 individual spectra for the entire 96MCA-MES. Representative impedance magnitude spectra and their analysis are shown in SI-Fig. 4. Notably, all six impedance spectra taken within a single microcavity exhibited the same shape and basic offset (SI-Fig. 4A), demonstrating the high accuracy of micro-electrode fabrication and positioning. The high comparability of all 576 spectra (SI-Fig. 4B and C) across the 96MCA-MES as well as the long-term stability of the 96MCA-MES (SI-Fig. 5) underlines the quality of the whole fabrication process.

To initially evaluate the EIS-based analysis of 3D objects, we utilized

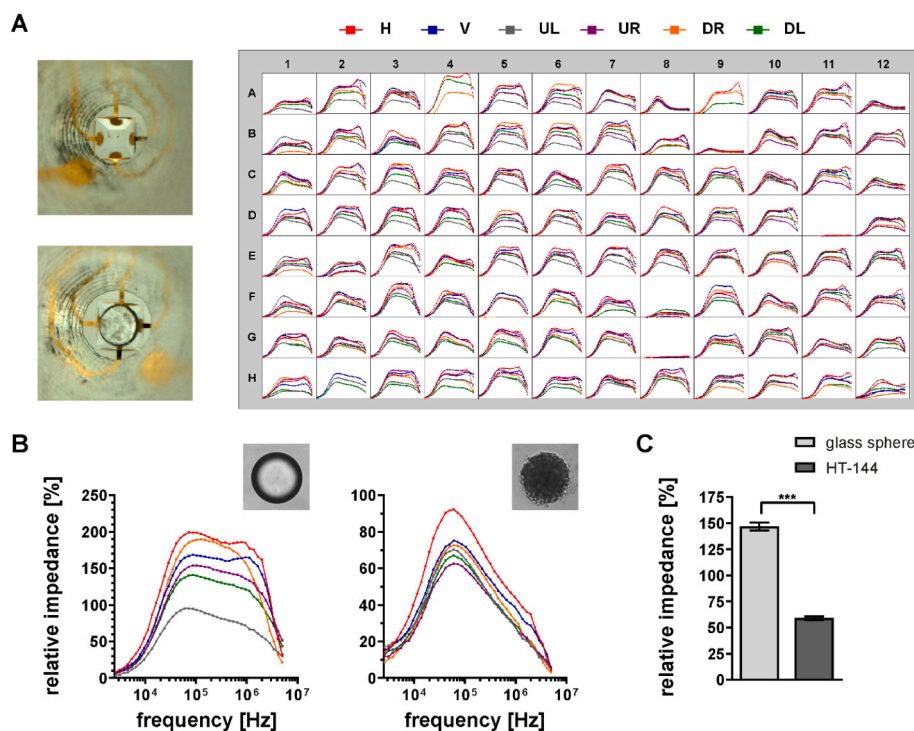


**Fig. 3.** Impedimetric characterization of the 96MCA-MES. (A) 576 relative impedance spectra of glass beads within one representative microcavity (images, left). Six relative impedance (2500–500000 Hz, uniform y-scale 0–300 %) spectra (image, right) were measured for each of the 96 microcavities filled with a glass bead, where the measuring directions of the electrodes were the following: opposite horizontal (H, red) and vertical (V, blue) as well as the electrode combinations across the corner (upper (U), left (L), right (R), down (D)); UL (grey), UR (purple), DR (orange), DL (green)). (B) Comparison of representative relative impedance spectra of a single glass sphere (left) and a single HT-144 spheroid (right). (C) Statistical analysis of the maximum relative impedance of glass spheres and HT-144 spheroids (mean  $\pm$  sem,  $n = 96$ , \*\*\* $p < 0.001$ ).

glass beads with a mean diameter of  $500 \pm 20 \mu\text{m}$  (Fig. 3). After the automated positioning of the glass beads, we determined and plotted all 576 relative impedance spectra (Fig. 3A). Differences between the impedance spectra of the individual glass beads could be detected and reflected the non-uniform size of the glass beads. Upon closer examination of the obtained spectra, it was evident that spectra exhibited a similar shape including a broad plateau in the frequency range between 3 kHz and 2 MHz. The spectra shape has been described previously for glass beads (Zitzmann et al., 2022). Differences in maximal relative impedance between the six spectra recorded within an individual microcavity holding a glass bead, is the result of different measurement paths between the electrodes (see SI-Fig. 4A for measurement profile). Here, spectra recorded between two adjacent electrodes had a lower maximum relative impedance, than those recorded between opposite electrodes (Fig. 3B).

In a next step, we analysed the baseline noise level and potential crosstalk between wells/microcavities (SI-Fig. 6). The observed noise levels below 0.5 % relative impedance up to 1 MHz (below 1 % above 1 MHz) do not represent a restriction with regard to the sensitive analysis of measurement objects (SI-Fig. 6A). Moreover, the crosstalk analysis of the baseline signal as well as on the measurement object signal also revealed deviations in the range of 0.5 % or less.

Based on these findings we continued with the evaluation of biological samples. In contrast to glass spheres, when analysing HT-144 spheroids as an example for a 3D cell culture, a more Gaussian spectra shape was observed, with less disparity in the spectra heights (Fig. 3B, right; SI-Fig. 7). The shape of the impedance spectra as well as the maximum relative impedance differed between glass beads and HT-144 spheroids. In two additional experiments, one with glass beads and one with HT-144 spheroids, 96 3D objects were analysed to evaluate the impedance differences. Thereby, the maximum relative impedance was  $146.76 \pm 3.7\%$  and  $59.15 \pm 1.86\%$  for glass spheres and HT-144

spheroids, respectively (Fig. 3C). Again, these values were in accordance with values determined previously with a smaller scaled MCA platform for the same objects (Zitzmann et al., 2022).

After initial evaluation, we used HT-144 spheroids for (long-term) stability testing as this cancer cell line is highly migrative and proliferative (SI-Fig. 8). To avoid spheroid attachment as well as cell outgrowth onto the electrodes and whole microcavity SU-8 was used as passivation layer, which offers a more hydrophobic surface than glass or other passivation materials like silicon nitride (Schmidt et al., 2021) and was further optimized by a plasma treatment. As a result, even after three days of continuous culturing, no spheroid attachment and disintegration or clear cell outgrowth could be observed by microscopic (SI-Fig. 8A) or impedimetric analysis (SI-Fig. 8B). Even more remarkable, the impedimetric monitoring of the 20 HT-144 spheroids revealed robust and stable monitoring over 72 h with highly viable spheroids at the end of experiment (SI-Fig. 8C).

In summary, the developed 96MCA-MES facilitates rapid bio-electronic analyses of 96 objects in parallel. Thanks to the high quality of microcavities the upscaling process did not result in any impedance signal reduction compared to systems with smaller number of cavities (Zitzmann et al., 2022), signal noise or crosstalk that could interfere with a robust and sensitive monitoring of spheroid cultures.

### 3.3. Integrated formation of 3D cultures and impedimetric drug effect monitoring with 96MCA-MES

To further integrate the 96MCA-MES into daily laboratory routines, we developed a plug-in for spheroid culture formation on-site, by following the approach of Hsiao et al. (Fig. 4A–SI-Fig. 9) (Hsiao et al., 2012). Here, we designed a hanging drop plug-in for the 96MCA-MES and fabricated it by SLA-3D-printing. The construction details are provided in SI-Fig. 9A. The add-on hanging-drop plug-in is filled with a cell

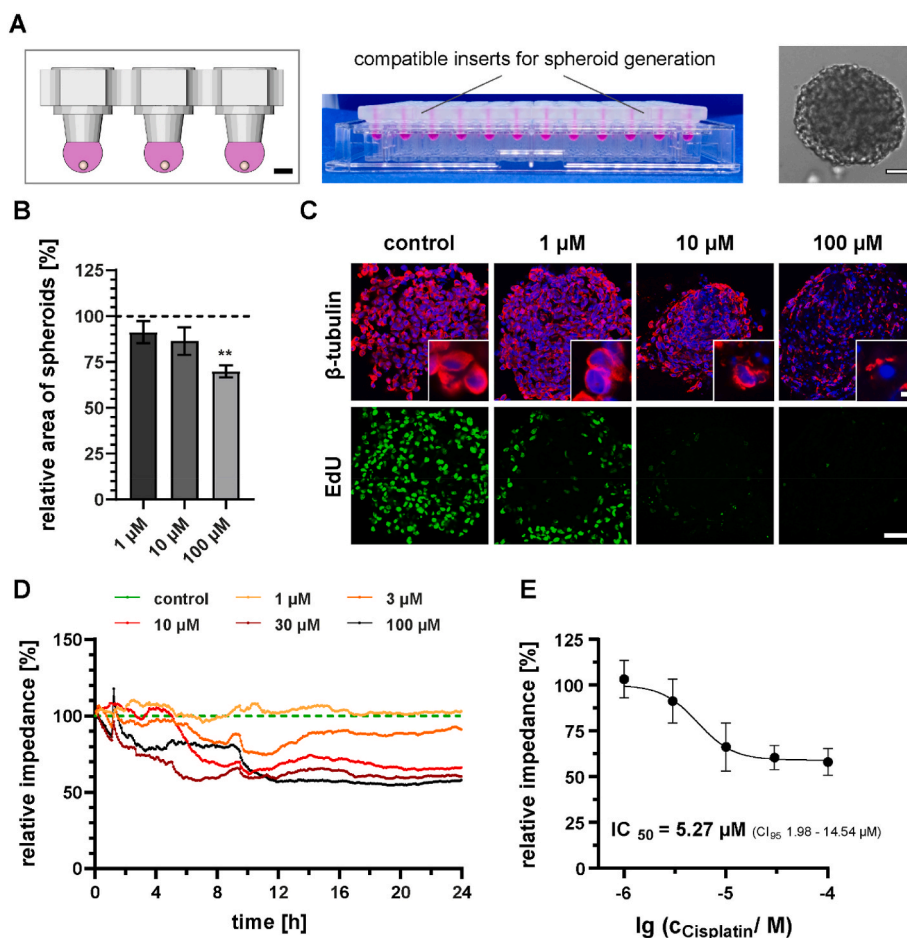


**Fig. 4.** Human melanoma spheroid formation and the effect of cisplatin on the resulting 3D cell culture over 24 h. (A) Left: Schematic view of the hanging drop method. Middle: The insert was filled with cell suspension on a microtiter plate. Right: Representative image of a HT-144 spheroid generated the insert system (scale: 100  $\mu\text{m}$ ). (B) Growth inhibition of the HT-144 spheroid by cisplatin shown as normalization to control (black dashed line, mean  $\pm$  sem,  $n = 16$ ). The bar plot shows the relative area increase of HT-144 spheroids normalization to control samples (black dashed line, mean  $\pm$  sem,  $n = 16$ ). (C) Immunocytochemical analysis of the HT-144 spheroids, where red and blue denote for  $\beta$ -tubulin, nuclear counter stain DAPI, respectively. Cell proliferation within the spheroids was evaluated in presence of increasing cisplatin with an EdU assay (green, scale: 50  $\mu\text{m}$ , magnification: 10  $\mu\text{m}$ ). (D) Relative impedance measured in the 96MCA-MES filled with HT-144 spheroids over time (normalized to the start of treatment and to the control concentration, average values over time,  $n = 8$  spheroids) and variation of the cisplatin concentration. (E) Concentration-response curve for cisplatin with the determined  $\text{IC}_{50}$  and 95% confidence interval ( $\text{CI}_{95}$ ) values (mean  $\pm$  sem,  $n = 8$ ).

suspension and then either placed on a standard microtiter plate or directly onto the 96MCA-MES (SI-Fig. 9B). The advantage of the plug-in is the elimination of the manual step of transferring and selecting spheroids by pipetting into the 96MCA-MES. Spheroids produced within the plug-in were comparable to spheroids formed under standard conditions as demonstrated in SI-Fig. 9D. In summary, this developed plug-in streamlined the pipetting process and thus represented a step towards fully automated analytical 3D cell culture systems.

Next, we employed HT-144 spheroids as a malignant melanoma cell model to showcase the capabilities of the 96MCA-MES (Fig. 4B–E). Therefore, we first characterized off-chip the effect of cisplatin, a chemotherapeutic drug, on the HT-144 spheroids over 24 h. Cisplatin's well-documented effect in the literature is based on its ability to bind to DNA, ultimately leading to the inhibition of DNA synthesis and cell growth (Barabas et al., 2008; Brown et al., 2019; Del Bello et al., 2013). Concentrations of 10–100  $\mu\text{M}$  led to inhibition of proliferation within HT-144 spheroids and resulted in cytoskeletal and cellular degeneration within 24 h, as depicted in Fig. 4B. Notably, spheroids were significantly smaller at a concentration of 100  $\mu\text{M}$  compared to the control group (normalized to control: 1  $\mu\text{M}$ :  $91.23 \pm 5.94\%$ , 10  $\mu\text{M}$ :  $86.42 \pm 7.52\%$ , 100  $\mu\text{M}$ :  $69.83 \pm 3.3\%$ ). Immunocytochemical analyses after 24 h of treatment with cisplatin revealed two effects: (i) Cisplatin induced a

spatial reordering of the protein  $\beta$ -tubulin, from a uniformly in absence to local aggregated spatial distribution in presence of cisplatin (see magnification in Fig. 4C). (ii) Cisplatin inhibited the proliferation of HT-144 cells as detected by the EdU assay (Fig. 4C). Repeating HT-144 spheroid stimulation experiment with cisplatin on the 96MCA-MES platform allowed to quantify cellular changes by electrochemical impedance spectroscopy (Fig. 4D/E, SI-Fig. 10). Thanks to the 96MCA-MES's advantage for parallel testing, we were able to analyse the effect of cisplatin at six concentrations with eight replicates in a single experiment. In detail, lower concentrations up to 3  $\mu\text{M}$  did not lead to significant effects after 24 hours of compound treatment compared to the control group, while concentrations of 10  $\mu\text{M}$ –100  $\mu\text{M}$  resulted in a clear decrease down to 60.3% (10  $\mu\text{M}$ ) and 57.6% (100  $\mu\text{M}$ ) of control values (Fig. 4D); which is statistically significant for 30  $\mu\text{M}$  and 100  $\mu\text{M}$  after 12 hours (SI-Fig. 10B). These findings align with a previous study that conducted impedimetric analysis on 3D cultures from melanoma biopsies, revealing comparable results for cisplatin concentrations of 10  $\mu\text{M}$ –100  $\mu\text{M}$  (Jahnke et al., 2014). Furthermore, the analysis of a concentration-response curve yielded an  $\text{IC}_{50}$  value of 5.27  $\mu\text{M}$  ( $\text{CI}_{95}$  1.98–14.54  $\mu\text{M}$ ) for cisplatin on HT-144 spheroids (Fig. 4E), which is consistent with the literature (Jahnke et al., 2014; Wroblewska-Luczka et al., 2021). In conclusion, the impedimetric analysis of

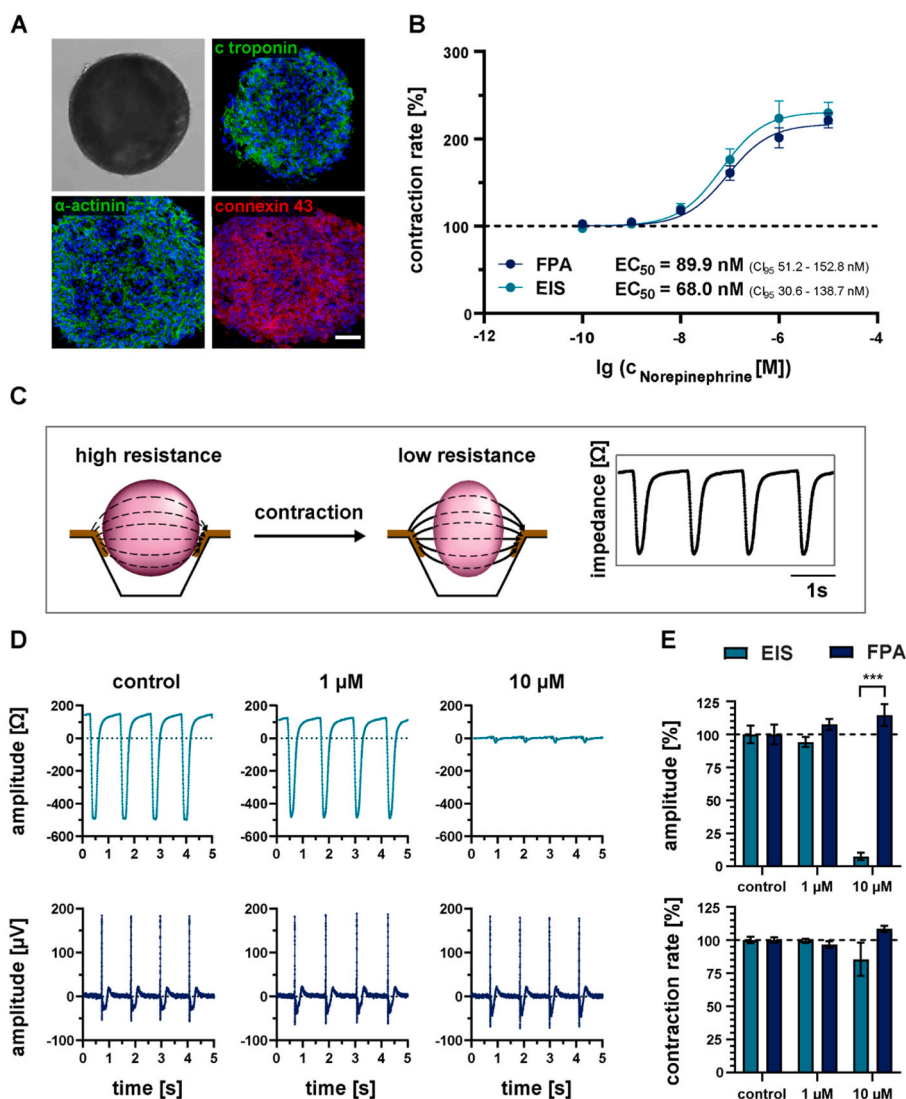


**Fig. 5.** Bioelectronic cardiotoxicity study on human cardiomyocyte clusters with norepinephrine and blebbistatin on the 96MCA-MES. (A) Image of a contractile human cardiomyocyte cluster (hCMC) with corresponding immunocytochemical analysis of the cardiac-specific markers c-troponin (green),  $\alpha$ -actinin (green) and the gap-junction protein connexin 43 (red). Nuclei are counterstained with DAPI (blue, scale: 100  $\mu$ m). (B) Bioelectronic analyses (FPM-field potential monitoring, EIS- electrochemical impedimetric analyses) of norepinephrine shown comparatively in concentration-response curves with indication of  $EC_{50}$  value and  $CI_{95}$  interval (mean  $\pm$  sem,  $n = 10$ ). (C) Schematic illustration of impedance analysis on contractile spheroids. Two contraction states with corresponding field lines and the resulting measurement profile. (D) Representative signal traces of real-time impedance and field potential measurement for the effect of 1 and 10  $\mu$ M blebbistatin on contractions of hCMCs. (E) Statistical analysis of the blebbistatin effect (mean  $\pm$  sem,  $n = 9$ ). Values of the statistical analysis (B/D) were normalized to controls.

cisplatin's effect on melanoma cells demonstrates the ease and reliability of using the 96MCA-MES for label-free and non-invasive long-term monitoring of 3D cell cultures.

### 3.4. Multimodal label-free monitoring of human cardiomyocyte 3D cultures and the effect of cardioactive substances

In the last step, we sought to demonstrate the capabilities of the 96MCA-MES by taking advantage of performing parallel field potential monitoring (FPM) and electrical impedance spectroscopy (EIS) on human cardiomyocytes cultured in 3D (Fig. 5). While action potentials of cardiomyocytes are detected by FPM, the contraction strength of the cardiomyocyte clusters is monitored by EIS (see Fig. 5C). To challenge the system, we used sensitive induced pluripotent stem cell-derived human cardiomyocytes (hCMCs). Spheroid-shaped hCMCs cultures, with a diameter of 500  $\mu$ m, were formed through separation and reaggregation, following a procedure previously described (Fleischer et al.,

2019). Spheroids contained a high-content of homogeneously distributed cardiomyocytes, as evidenced by the presence of cardiac structural proteins like c-troponin and  $\alpha$ -actinin, as well as functional syncytium connections, confirmed by the gap-junction marker connexin 43 (Fig. 5A). hCMCs exhibit spontaneous contractions, resembling physiological *in vivo* conditions (see SI-Movie). With the 96MCA-MES we performed a combined FPM and EIS monitoring on hCMCs. In this context, we first proved that there is also no crosstalk for FPM between microcavities/wells (SI-Fig. 6B). For impedance measurement the frequency was kept constant at 100 kHz enabling a rate of 600 samples per second, which allows highly temporal resolved traces of the hCMC contraction mechanic. During the inhibition of mechanical contraction, hCMCs remain in close proximity to the electrode, resulting in no significant change in the impedance amplitude on the (sub)second time scale (Fig. 5C). To demonstrate the capabilities for robust parallel monitoring with both monitoring techniques, we placed 96 individual hCMCs in the 96MCA-MES, whereby we could detect signals from

almost all of them (SI-Fig. 11).

Based on this, we started with testing the effects of norepinephrine, a substance known to increase the contraction rate of cardiac cells (Böhm et al., 1995; Jahnke et al., 2013). Norepinephrine was applied to the hCMCs at concentrations ranging from 0.1 nM to 10  $\mu$ M (Fig. 5B). From the acquired FPM and EIS values, we constructed two concentration-response curves to determine the corresponding EC<sub>50</sub> values. Strikingly, the EC<sub>50</sub> values obtained from the cardiomyocytes contractions and detected action potentials were comparable with 89.9 nM and 68 nM for FPA and EIS, respectively. Subsequently, we analysed the impact of blebbistatin on hCMCs. (S)-Blebbistatin is an ATPase inhibitor that selectively targets myosin II and inhibits cardiac cluster contractility, without affecting the action potential (Fedorov et al., 2007; Kovacs et al., 2004; Roman et al., 2018). The effect of 1 and 10  $\mu$ M blebbistatin was compared to a control cell culture (Fig. 5D). The spectra from a representative electrode obtained through FPM and EIS illustrated that 1  $\mu$ M blebbistatin had no effect on the contraction frequency of hCMCs. However, 10  $\mu$ M blebbistatin resulted in a significant reduction in mechanical contractions, as indicated by the lower EIS amplitudes (Fig. 5E). Notably, FPM analyses revealed that action potentials were still generated. Our result that blebbistatin decreased the contractility of hCMCs without detectable effect on electrophysiology is in accordance to previous findings for blebbistatin measured on stem cell-derived mouse cardiomyocytes in 2D cell cultures (Abassi et al., 2012). In summary, using these two cardioactive substances, we have demonstrated that the newly developed 96MCA-MES, in combination with the positioning insert, enables multimodal label-free analysis of sensitive 3D human cultures through rapid positioning in the microcavities and parallel analyses using EIS and FPM.

#### 4. Conclusion

In summary, we have engineered a new microcavity-based cell culture system with a multi-microelectrode system to enable label-free analysis of 96 3D cell cultures. The system was fabricated by applying a three-step fabrication process, which involves a SLE glass structuring step, build-up of microelectrodes by a lift-off process step, and a bonding step to contact the microelectrodes to a PCB frame and microcavities to a plastic cell culture well-plate.

During the characterization of the 96MCA-MES, we demonstrated that it is possible to record 576 individual EIS spectra from each of the 96 glass spheres or cell cultures positioned in the individual microcavities. The impedimetric characterization of the 96MCA-MES with glass beads and different 3D cell culture models showed that the upscaling of a MCA does not limit bioelectrical analyses in the frequency range up to 5 MHz nor does it lead to signal noise or crosstalk, which could impair a sensitive multimodal analysis of 3D cultures.

To overcome automatization limitations, we further developed a plug-in for positioning 3D objects into the microcavities. With the plug-in we achieved fill rates of 96%. Although the plug-in positioning tool as well as the microcavity was optimized for 3D cell cultures with a mean diameter of 500  $\mu$ m, the SLE technology and the SLA-3D-printing method allow rapid adaptation of the system to other spheroid sizes, and cell type models. In this regard, we developed an additional plug-in to integrate the formation of 3D cell cultures by the hanging drop method within the 96MCA-MES. The two developed plug-ins together are significant steps toward automating bioelectronic analysis of 3D cell cultures.

Using the HT-144 melanoma and hCMC cell models, we demonstrated a wide range of monitoring applications for biological parameters like cell proliferation, degeneration, contraction and cellular electrophysiology as well as drug effects on these parameters. Taken together, this illustrates the significant advantage of our system for the label-free, non-invasive and continuous real-time high-content based screening of 3D cultures over hours or days. In order to present the advantages once again in a focussed and concrete way, we have

compared this with the few systems or alternatives that are available for monitoring spheroidal 3D cultures (SI-Table 3). Notably, the described 96MCA-MES is limited by the number of conductive tracks, contact pads, and subsequent electronic contacts. Conceptually new technical solutions are needed to overcome this limitation in future studies to increase resolution (Zitzmann et al., 2022). Overall, the 96MCA-MES has proven its applicability for high-throughput multiparametric analysis of drugs in human 3D cell cultures, such as hCMCs, bringing us closer to drug development and clinical diagnosis compared to previously described systems.

#### CRedit authorship contribution statement

**Franziska D. Zitzmann:** Writing – review & editing, Writing – original draft, Visualization, Validation, Methodology, Investigation, Formal analysis. **Sabine Schmidt:** Writing – original draft, Methodology, Investigation. **Ronny Frank:** Visualization, Validation, Methodology, Investigation. **Winnie Weigel:** Methodology, Investigation. **Matthias Meier:** Writing – review & editing, Writing – original draft, Resources. **Heinz-Georg Jahnke:** Writing – review & editing, Writing – original draft, Visualization, Supervision, Methodology, Investigation, Funding acquisition, Formal analysis, Conceptualization.

#### Declaration of competing interest

The authors declare that they have no known competing financial interests or personal relationships that could have appeared to influence the work reported in this paper.

#### Data availability

Data will be made available on request.

#### Acknowledgements

This work was funded by the Federal Ministry of Education and Research of Germany (BMBF) [project: “SaxoCell Systems” Grant No. 03ZU1111NC], the Federal Ministry for Economics Affairs and Climate Action of Germany (BMWK) [project: “STARK: b-ACTmatter” Grant No. 46SKD023X], the European Union (EFRE) and the Saxon Ministry of Science and the Fine Arts (SMWK) [project: “CardioEpix”, Grant No. 100685579] and is tax-supported on the basis of the budget approved by the members of the parliament of the Free State of Saxony. The SLE device was funded by the Saxon Ministry of Science and the Fine Arts (SMWK) [project LasMino grant number: 100299999]. We thank Tobias Haensch and Christoph Prönnecke for stem cell culture assistance.

#### Appendix A. Supplementary data

Supplementary data to this article can be found online at <https://doi.org/10.1016/j.bios.2024.116042>.

#### References

- Abassi, Y.A., Xi, B., Li, N., Ouyang, W., Seiler, A., Watzle, M., Kettenhofen, R., Bohlen, H., Ehlich, A., Kolossov, E., Wang, X., Xu, X., 2012. *Br. J. Pharmacol.* 165 (5), 1424–1441.
- Barabas, K., Milner, R., Lurie, D., Adin, C., 2008. *Vet. Comp. Oncol.* 6 (1), 1–18.
- Böhm, M., La Rosée, K., Schwinger, R.H., Erdmann, E., 1995. *J. Am. Coll. Cardiol.* 25 (1), 146–153.
- Brown, A., Kumar, S., Tchounwou, P.B., 2019. *J. Cancer Sci. Ther.* 11 (4).
- Butkutė, A., Baravykas, T., Stančikas, J., Tickūnas, T., Vargalis, R., Paipulas, D., Sirutkaitis, V., Jonušauskas, L., 2021. *Opt Express* 29 (15), 23487–23499.
- Chan, M.V., Armstrong, P.C., Warner, T.D., 2018. *Platelets* 29 (7), 650–655.
- Costa, E.C., Moreira, A.F., de Melo-Diogo, D., Gaspar, V.M., Carvalho, M.P., Correia, L.J., 2016. *Biotechnol. Adv.* 34 (8), 1427–1441.
- Del Bello, B., Toscano, M., Moretti, D., Maellaro, E., 2013. *PLoS One* 8 (2), e57236.
- Eichler, M., Jahnke, H.G., Krinke, D., Müller, A., Schmidt, S., Azendorf, R., Robitzki, A., 2015. *Biosens. Bioelectron.* 67, 582–589.

- Erdmann, S., Seidel, D., Jahnke, H.G., Eichler, M., Simon, J.C., Robitzki, A.A., 2019. *Sci. Rep.* 9 (1), 30.
- Fedorov, V.V., Lozinsky, I.T., Sosunov, E.A., Anyukhovskiy, E.P., Rosen, M.R., Balke, C. W., Efimov, I.R., 2007. *Heart Rhythm* 4 (5), 619–626.
- Fleischer, S., Jahnke, H.G., Fritsche, E., Girard, M., Robitzki, A.A., 2019. *Biosens. Bioelectron.* 126, 624–631.
- Gottmann, J., Hermans, M., Repiev, N., Ortmann, J., 2017. *Micromachines* 8 (4), 110.
- Guo, L., Abrams, R.M., Babiarz, J.E., Cohen, J.D., Kameoka, S., Sanders, M.J., Chiao, E., Kolaja, K.L., 2011. *Toxicol. Sci.* 123 (1), 281–289.
- Habanjar, O., Diab-Assaf, M., Caldefie-Chezet, F., Delort, L., 2021. *Int. J. Mol. Sci.* 22 (22).
- Hsiao, A.Y., Tung, Y.C., Kuo, C.H., Mosadegh, B., Bedenis, R., Pienta, K.J., Takayama, S., 2012. *Biomed. Microdevices* 14 (2), 313–323.
- Jahnke, H.G., Krinke, D., Seidel, D., Lilienthal, K., Schmidt, S., Azendorf, R., Fischer, M., Mack, T., Striggow, F., Althaus, H., Schober, A., Robitzki, A.A., 2017. *Biosens. Bioelectron.* 88, 78–84.
- Jahnke, H.G., Poenick, S., Maschke, J., Kendler, M., Simon, J.C., Robitzki, A.A., 2014. *Cancer Res.* 74 (22), 6408–6418.
- Jahnke, H.G., Steel, D., Fleischer, S., Seidel, D., Kurz, R., Vinz, S., Dahlenborg, K., Sartipy, P., Robitzki, A.A., 2013. *PLoS One* 8 (7), e68971.
- Kloss, D., Kurz, R., Jahnke, H.G., Fischer, M., Rothermel, A., Anderegg, U., Simon, J.C., Robitzki, A.A., 2008. *Biosens. Bioelectron.* 23 (10), 1473–1480.
- Kovacs, M., Toth, J., Hetenyi, C., Malnasi-Csizmadia, A., Sellers, J.R., 2004. *J. Biol. Chem.* 279 (34), 35557–35563.
- LaBarbera, D.V., Reid, B.G., Yoo, B.H., 2012. *Expet Opin. Drug Discov.* 7 (9), 819–830.
- Lopez, C.M., Chun, H.S., Wang, S., Berti, L., Putzeys, J., Bulcke, C.V.D., Weijers, J.W., Firrincieli, A., Reumers, V., Braeken, D., Helleputte, N.V., 2018. *IEEE J. Solid State Circ.* 53 (11), 3076–3086.
- Mulder, P., de Korte, T., Dragicevic, E., Kraushaar, U., Printemps, R., Vlaming, M.L.H., Braam, S.R., Valentin, J.P., 2018. *J. Pharmacol. Toxicol. Methods* 91, 36–42.
- Pinto, B., Henriques, A.C., Silva, P.M.A., Bousbaa, H., 2020. *Pharmaceutics* 12 (12), 1186.
- Poenick, S., Jahnke, H.G., Eichler, M., Frost, S., Lilie, H., Robitzki, A.A., 2014. *Biosens. Bioelectron.* 53, 370–376.
- Roman, B.I., Verhasselt, S., Stevens, C.V., 2018. *J. Med. Chem.* 61 (21), 9410–9428.
- Schmidt, S., Frank, R., Krinke, D., Jahnke, H.G., Robitzki, A.A., 2022. *Biosens. Bioelectron.* 202, 114012.
- Schmidt, S., Haensch, T., Frank, R., Jahnke, H.G., Robitzki, A.A., 2021. *ACS Appl. Mater. Interfaces* 13 (49), 59185–59195.
- Scott, C.W., Peters, M.F., 2010. *Drug Discov. Today* 15 (17–18), 704–716.
- Wang, A., Madden, L.A., Paunov, V.N., 2020. *J. Mater. Chem. B* 8 (46), 10487–10501.
- Wroblewska-Luczka, P., Grabarska, A., Florek-Luszczki, M., Plewa, Z., Luszczki, J.J., 2021. *Int. J. Mol. Sci.* 22 (2).
- Zitzmann, F.D., Jahnke, H.G., Nitschke, F., Beck-Sickinger, A.G., Abel, B., Belder, D., Robitzki, A.A., 2017. *Lab Chip* 17 (24), 4294–4302.
- Zitzmann, F.D., Schmidt, S., Naumann, M., Belder, D., Jahnke, H.G., Robitzki, A.A., 2022. *Biosens. Bioelectron.* 202, 114010.